

# Ferroelectric-Modulated MoS<sub>2</sub> Field-Effect Transistors as Multilevel Nonvolatile Memory

Liping Xu,<sup>1</sup> Zhihua Duan,<sup>1</sup> Peng Zhang, Xiang Wang, Jinzhong Zhang,\* Liyan Shang, Kai Jiang, Yawei Li, Liangqing Zhu, Yongji Gong, Zhigao Hu,\* and Junhao Chu



Cite This: *ACS Appl. Mater. Interfaces* 2020, 12, 44902–44911



Read Online

ACCESS |



Metrics & More



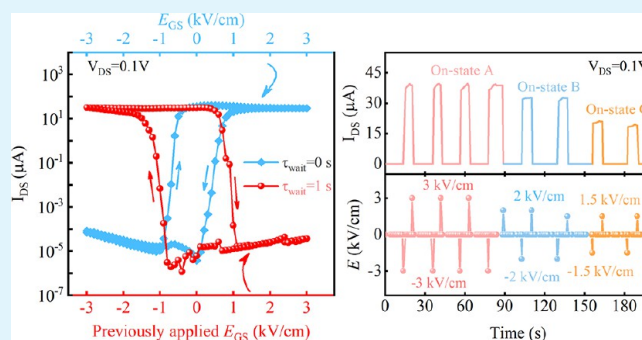
Article Recommendations



Supporting Information

**ABSTRACT:** Ferroelectric field-effect transistors (FeFETs) with semiconductors as the channel material and ferroelectrics as the gate insulator are attractive and/or promising devices for application in nonvolatile memory. In FeFETs, the conductivity states of the semiconductor are utilized to explore the polarization directions of the ferroelectric material. Herein, we report FeFETs based on a few layers of MoS<sub>2</sub> on a 0.7Pb(Mg<sub>1/3</sub>Nb<sub>2/3</sub>)O<sub>3</sub>–0.3PbTiO<sub>3</sub> (PMN–PT) single crystal with switchable multilevel states. It was found that the On–Off ratios can reach as high as 10<sup>6</sup>. We prove that the interaction effect of ferroelectric polarization and interface charge traps has a great influence on the transport behaviors and nonvolatile memory characteristics of MoS<sub>2</sub>/PMN–PT FeFETs. In order to further study the underlying physical mechanism, we have researched the time-dependent electrical properties in the temperature range from 300 to 500 K. The separation of effects from ferroelectric polarization and interfacial traps on electrical behaviors of FeFETs provides us with an opportunity to better understand the operation mechanism, which suggests a fantastic way for multilevel, low-power consumption, and high-density nonvolatile memory devices.

**KEYWORDS:** MoS<sub>2</sub>, PMN–PT single crystal, ferroelectric field-effect transistor, multilevel memory, hysteresis



switched.<sup>22</sup> Contemporarily, ferroelectrics have an increasing extensive application in many fields, for instance ferroelectric random access memories (FeRAM) for nonvolatile data storage<sup>23</sup> and ferroelectric field-effect transistors (FeFETs) for nonvolatile memory with low-power consumption.<sup>24–26</sup> FeRAM builds a one–transistor–one–capacitor cell by a ferroelectric capacitor. However, in FeRAM devices, the reading process is destructive, because in order to detect the polarization direction of the ferroelectric material, a pulsed voltage whose amplitude is higher than the coercive voltage has to be applied. Therefore, after each reading operation, the data bit needs to be reset, leading to a large readout time and high power consumption. The structure mentioned above has been commercialized, but its market share is limited. In a FeFET, the channel and gate insulator are made of a semiconductor and a ferroelectric material, respectively. The read operation is carried out by testing the channel conductance, which can determine the polarization direction of the ferroelectric gate

## 1. INTRODUCTION

Two-dimensional (2D) atomically thin transition metal dichalcogenides (TMDs) have recently attracted considerable interest, owing to the potential to manufacture multifarious function devices within the limit of atomic thickness, such as electronics,<sup>1–4</sup> optics,<sup>5–10</sup> catalysis,<sup>11–14</sup> and sensors.<sup>15</sup> Unlike graphene, 2D materials whose chemical formula is MX<sub>2</sub> are characterized by layered structures, where M and X represent transition metal and chalcogens, respectively. For 2D TMDs, interlayer van der Waals interplay is feeble, while the intralayer covalent bonding of X–M–X is strong.<sup>16,17</sup> As a representative member of the TMD family, MoS<sub>2</sub> in the form of a monolayer shows a direct band gap of 1.80 eV, and in blocky MoS<sub>2</sub>, the band gap becomes indirect with the value of 1.2 eV.<sup>18,19</sup> MoS<sub>2</sub> has revealed its significant meaning in fundamental investigations and widespread applications. Due to ultrahigh area-to-volume ratio, 2D TMDs are quite sensitive to an external stimulus, making them appropriate for constructing heterostructures with three-dimensional (3D) thick films and/or one-dimensional (1D) nanowires.<sup>20</sup>

Ferroelectrics (FEs) commonly refer to the materials, which have a spontaneous polarization and a large dielectric constant simultaneously.<sup>21</sup> Thereinto, according to ion displacement of the crystal, the polarization can be redirected. Under the action of an external electric field, the direction of polarization can be

switched.<sup>22</sup> Contemporarily, ferroelectrics have an increasing extensive application in many fields, for instance ferroelectric random access memories (FeRAM) for nonvolatile data storage<sup>23</sup> and ferroelectric field-effect transistors (FeFETs) for nonvolatile memory with low-power consumption.<sup>24–26</sup> FeRAM builds a one–transistor–one–capacitor cell by a ferroelectric capacitor. However, in FeRAM devices, the reading process is destructive, because in order to detect the polarization direction of the ferroelectric material, a pulsed voltage whose amplitude is higher than the coercive voltage has to be applied. Therefore, after each reading operation, the data bit needs to be reset, leading to a large readout time and high power consumption. The structure mentioned above has been commercialized, but its market share is limited. In a FeFET, the channel and gate insulator are made of a semiconductor and a ferroelectric material, respectively. The read operation is carried out by testing the channel conductance, which can determine the polarization direction of the ferroelectric gate

Received: June 1, 2020

Accepted: September 15, 2020

Published: September 15, 2020



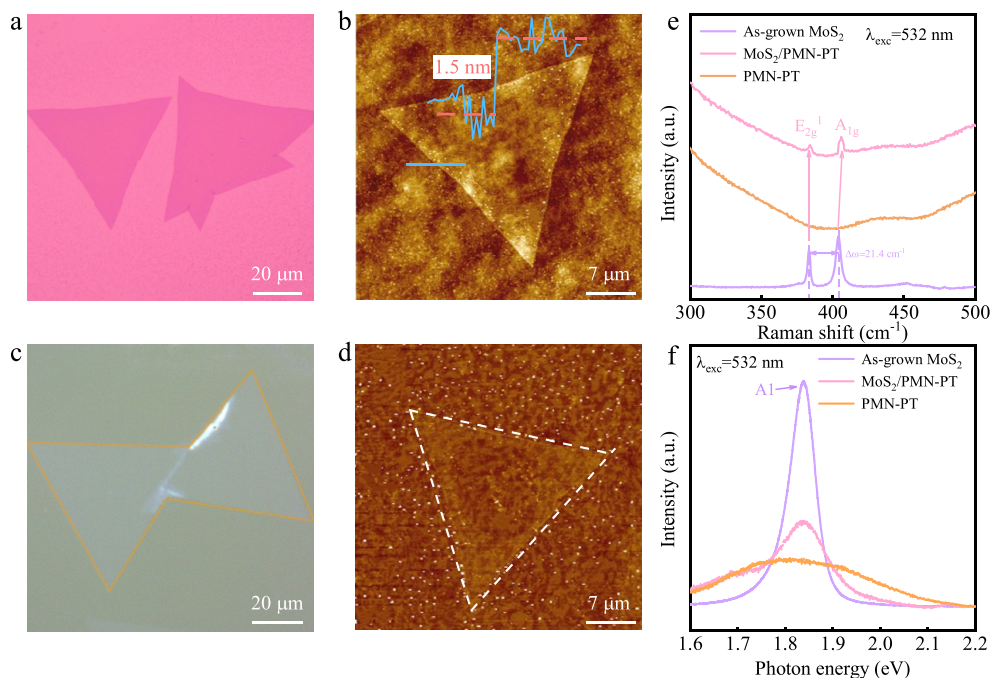


**Figure 1.** (a) Optical microscope photograph of MoS<sub>2</sub> flakes grown on a Si/SiO<sub>2</sub> substrate. (b) Topography image of a synthetic bilayer MoS<sub>2</sub>. Cross-sectional height profile was presented in the inset. (c) The typical optical micrograph and (d) the corresponding topography image of MoS<sub>2</sub> transferred onto the PMN–PT substrate. Yellow and white dotted lines are used to highlight the MoS<sub>2</sub> flakes. (e) Raman spectra and (f) PL spectra of the MoS<sub>2</sub> flakes before and after being transferred onto PMN–PT substrates as well as the Raman and PL spectra of the PMN–PT.

insulator, resulting in a nondestructive reading process in FeFETs. Therefore, FeFET-based RAM has the advantages of the fast switching speed of polarization in ferroelectric materials,<sup>27</sup> nondestructive reading operation, nonvolatile storage state, and concise configuration for high-density integration, making it a promising memory technology.

The synergy effect between materials with different functionalities and dimensionalities may be an issue in new physical properties and device applications. Particularly, there is an extensive interest in electronic devices, in which a 2D TMD semiconductor coupled with a ferroelectric material serve as the channel and gate dielectric layer, respectively. In addition to chemical vapor deposition (CVD) and mechanical exfoliation (ME), the 2D TMD layer can be prepared by the liquid metal method. According to the liquid metal method, the self-exfoliation of the prepared 2D TMDs can be realized by taking advantage of their nonpolar nature.<sup>28,29</sup> Previously, MoS<sub>2</sub>-based FETs have been reported with an organic ferroelectric polymer poly(vinylidene fluoride-trifluoroethylene) (P(VDF-TrFE)) as the top dielectric for nonvolatile memory<sup>30</sup> and photodetectors.<sup>31</sup> However, compared to inorganic FeFETs, the slow dipole dynamics and low mechanical and thermal durability of organic FeFETs restrict its applicability. Recently, inorganic FeFETs interfacing MoS<sub>2</sub> and WSe<sub>2</sub> with Pb(Zr<sub>x</sub>Ti<sub>1-x</sub>)O<sub>3</sub> (PZT) films have been investigated. However, the transport properties of the inorganic FeFETs are not as good as the FeFETs based on thin film, especially in the field of the On–Off ratio. Moreover, it is worth mentioning that the clockwise direction of transport hysteresis in FeFETs is contrary to the direction of the ferroelectric polarization loop. The interaction between ferroelectric polarization and interfacial charge traps has been investigated by time-reliant investigations in MoS<sub>2</sub>–PZT FETs<sup>32</sup> and graphene–0.7Pb(Mg<sub>1/3</sub>Nb<sub>2/3</sub>)O<sub>3</sub>–0.3PbTiO<sub>3</sub>.<sup>36</sup>

However, the investigations about how ferroelectric polarization may intuitively affect the electrical properties of the channel in a broad temperature range are rarely reported. The origin of the unexpected large clockwise behavior by FE gating has attracted extensive attention. Moreover, the ultimate mechanisms for store operation across the interfaces between the 2D TMD layer and FE are still unclear.<sup>24,32,33</sup> Thus, it is important to comprehend the nature of the effect in devices involving 2D TMD semiconductors combined with ferroelectric materials. Additionally, the reported FeFET-based nonvolatile memories are only worked by a single electrical stimulus, which limits their versatility and storage capacity.

Herein, we demonstrate multilevel nonvolatile memory devices adopting CVD grown MoS<sub>2</sub> flakes as the channel and monocrystal 0.7Pb(Mg<sub>1/3</sub>Nb<sub>2/3</sub>)O<sub>3</sub>–0.3PbTiO<sub>3</sub> (PMN–PT) as the gate dielectric. The monocrystal PMN–PT possesses a large remanent polarization and low coercive field ( $E_C$ ). The interfacial charges strongly affect the transport hysteresis in MoS<sub>2</sub>/PMN–PT FeFETs, and a reversed hysteresis loop is observed when the interfacial charges dissipate. This work shows that understanding the underlying physical mechanism is crucial for devices combining 2D TMDs with ferroelectric materials. The combined effects between interface charge traps and ferroelectric polarization on the transport properties and storage features for MoS<sub>2</sub>/PMN–PT FeFETs have been investigated by temperature-dependent electrical performance. Multilevel conductance states with electric excitation have been demonstrated at variable temperatures, which paves the way for novel high-density storage technology.

## 2. MATERIALS AND METHODS

**2.1. Growth of MoS<sub>2</sub> Layers.** MoS<sub>2</sub> nanosheets were prepared via the CVD method. Molybdenum trioxide (MoO<sub>3</sub>, 99.999% pure, Sigma-Aldrich) and sulfur (S, 99.99% pure, Sigma-Aldrich) powder

are used as the precursors. In particular, the precursor powder MoO<sub>3</sub> (3 mg) and 0.5 mg of NaCl were mixed together first. The alumina boat containing precursor powder was situated in the center of the heating zone. Si substrates with a 285 nm top layer of SiO<sub>2</sub> with the polished surface down were placed on top of the precursor powders. The heating zone center was heated to 650 °C (heating rate: 50 °C min<sup>-1</sup>) and maintained for 3 min. 100 mg of S was loaded in a secondary heating zone at the upstream side, and the temperature of the secondary heating zone center was kept at 200 °C for 3 min to prepare MoS<sub>2</sub>. Argon (Ar) flow was employed to transport the vaporized S to MoO<sub>3</sub> with a rate of 80 sccm. An atmospheric pressure in the furnace was maintained during the entire growth process.

**2.2. Fabrication of Devices.** To fabricate FeFETs, a few layers of MoS<sub>2</sub> flakes grown by CVD were transferred onto monocrystal PMN–PT substrate with (001) orientation and a thickness of 0.5 mm by a conventional PMMA-mediated method. The Ni/Au (2/50 nm) electrodes were made on MoS<sub>2</sub> flakes using a conventional procedure, namely, electron beam lithography (EBL), the thermal evaporator, and subsequent lift-off techniques. Finally, on the other surface of the PMN–PT substrate, the Ni/Au (2/50 nm) metals were straight evaporated via the thermal evaporator as the gate electrodes.

**2.3. Characterizations.** The synthesized MoS<sub>2</sub> was represented by optical microscopy (OM), atomic force microscopy (AFM), and Raman spectroscopy. A commercial AFM system (Dimension Icon, Bruker) was employed to characterize the surface topography of the CVD-grown MoS<sub>2</sub> flakes before and after transferring onto PMN–PT. A confocal micro-Raman spectrometer (LabRAM HR Evolution, Horiba Jobin-Yvon) in the backscattering geometry was used to carry out the Raman and photoluminescence (PL) spectra. The wavelength of the argon ion laser line is 532 nm. A 50× objective lens whose working distance is 18 mm was provided to focus the laser beam on the few-layer samples. The transport measurements were performed by an accurate semiconductor parameter analyzer Keithley 4200-SCS. The test temperature can range from 300 to 500 K in a cryogenic probe station Janis ST-500 in this work. A high vacuum with a pressure of 10<sup>-6</sup> Torr in the measurement chamber ensured the stability during the whole test process.

### 3. RESULTS AND DISCUSSION

Figure 1a,b presents the OM micrograph and AFM image of MoS<sub>2</sub> flakes grown on the Si/SiO<sub>2</sub> substrate. According to the height file, the MoS<sub>2</sub> nanosheet has a thickness of ~1.5 nm, as measured by AFM. Figure 1c,d illustrates the typical OM and the corresponding AFM micrograph of MoS<sub>2</sub> flakes transferred onto the PMN–PT substrate. In Figure 1a, the triangular shape of the MoS<sub>2</sub> nanosheets can be obviously identified. In Figure 1c, yellow dashed lines are used to highlight the MoS<sub>2</sub> flakes on the PMN–PT substrate. The typical lateral size of the MoS<sub>2</sub> triangle is about 60 μm. The optical and AFM images reveal the uniformity and continuity of MoS<sub>2</sub> flakes transferred onto the PMN–PT substrate. Figure 1e,f summarizes the Raman and PL spectra obtained from MoS<sub>2</sub> prepared on the Si/SiO<sub>2</sub> substrate and transferred onto the PMN–PT substrate. The Raman spectra reveal the existence of two active modes at 383.1 and 404.2 cm<sup>-1</sup>, which are assigned to E<sub>2g</sub><sup>1</sup> mode and A<sub>1g</sub> mode, respectively. The frequency difference Δω between two active modes A<sub>1g</sub> and E<sub>2g</sub><sup>1</sup> has been generally utilized as a sign of the thickness of the MoS<sub>2</sub> flake.<sup>34,35</sup> The Δω is 21.1 cm<sup>-1</sup> for bilayer MoS<sub>2</sub> grown on Si/SiO<sub>2</sub>, which is consistent with the result observed by AFM. However, after transfer onto a PMN–PT single crystal, the A<sub>1g</sub> mode appears to have considerable hardening, as much as 2 cm<sup>-1</sup>, while the E<sub>2g</sub><sup>1</sup> mode can be scarcely influenced by the substrate. The A<sub>1g</sub> mode is closely related to the out-of-plane motion of the S atoms relative to the Mo atoms. Thus, the hardening of the A<sub>1g</sub> mode can be linked to the variation in the dipolar interaction

strength between MoS<sub>2</sub> flakes and the fixed charges in different substrates. Apart from the Raman frequencies, the crystalline quality of MoS<sub>2</sub> can also be determined by the full width at half-maximum (FWHM) of the E<sub>2g</sub><sup>1</sup> peak.<sup>35</sup> The FWHM of the E<sub>2g</sub><sup>1</sup> mode for the as-grown and transferred MoS<sub>2</sub> bilayer are 2.98 and 2.82 cm<sup>-1</sup>, respectively, indicating that the transfer process has a minimal influence on the crystalline quality of the MoS<sub>2</sub>. The PL spectra show a peak at 1.84 eV, which is corresponding to A1 direct excitonic transition, i.e., optical direct transition from the κ point of the conduction band to valence band. The PL intensity of MoS<sub>2</sub> transferred onto PMN–PT seems to have a degradation. In order to compare quantitatively the PL spectra of MoS<sub>2</sub> obtained on different substrates, the optical interference and absorption effects need to be taken into account. For both the incident and the emitted light, optical interference can be induced by the different thickness and optical constants of the MoS<sub>2</sub> and substrate. Thus, the PL intensity can be affected by the interference induced by the substrate. However, the substrate induced interferometric situation barely perturbs the peak position of emission, while having a strong influence on the intensity of the emission.<sup>35</sup> The Raman and PL characteristics of MoS<sub>2</sub> transferred onto the PMN–PT substrate indicate that the MoS<sub>2</sub> flakes are not structurally strained or dramatically damaged by the transfer process.<sup>24</sup>

Details about the fabrication of MoS<sub>2</sub>/PMN–PT FeFETs with bottom-gate configuration are provided in the **Materials and Methods** section. Figure 2a presents the false-color optical

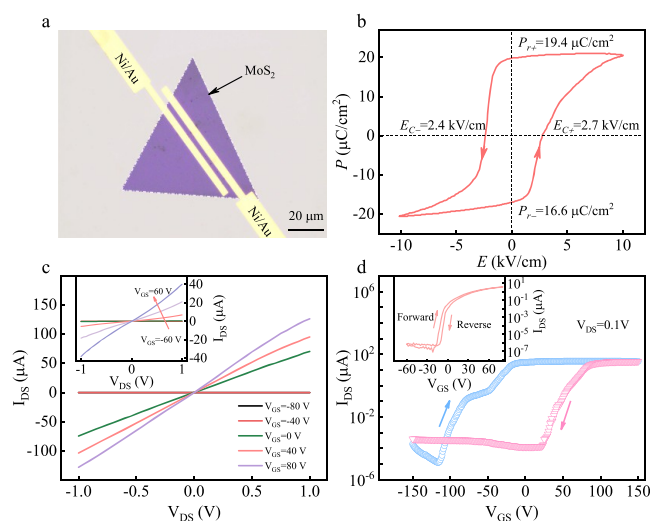


**Figure 2.** (a) False-color microscope photograph of the MoS<sub>2</sub>/PMN–PT FeFET device. (b) The polarization–electric field (*P*–*E*) curve of a ferroelectric capacitor (Ni/Au/PMN–PT/Ni/Au) structure. (c) Output characteristic curves and (d) transfer characteristic curve for the MoS<sub>2</sub>/PMN–PT device. The directions of the hysteresis loops are indicated by arrows. The output and transfer characteristic curves of MoS<sub>2</sub> on the Si/SiO<sub>2</sub> substrate are plotted in the insets in (c) and (d), respectively.

micrograph of a typical FeFET with a 5 μm width channel. The curve between the polarization *P* and external electric field *E* of PMN–PT measured by a capacitor composed of Ni/Au/PMN–PT/Ni/Au is shown in Figure 2b. For the forward sweeping, the polarization *P* of the PMN–PT single crystal starts to change at around *E* = 1.4 kV/cm and reaches saturation at around 7.5 kV/cm, while it remains unchanged

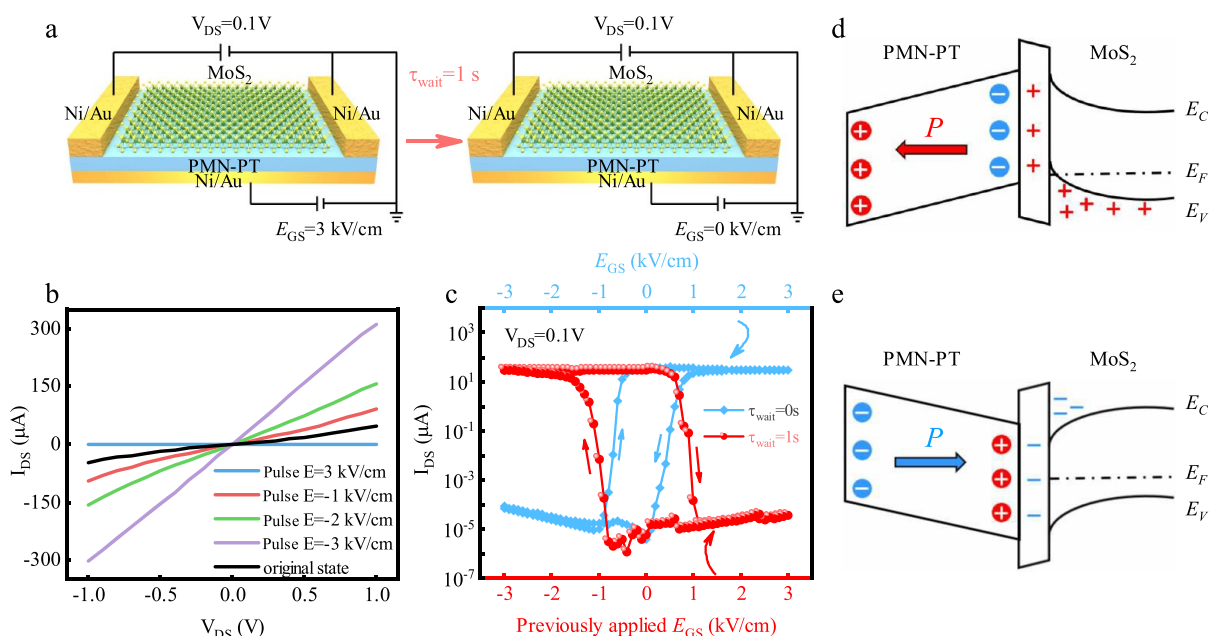


**Figure 3.** (a) Schematic diagram of the electrical measurements in MoS<sub>2</sub>/PMN-PT FeFETs. (b) Output curves of MoS<sub>2</sub>/PMN-PT FeFETs measured in up and down polarization states at  $V_{GS} = 0$  V. (c) Transfer curves of the architecture shown in (a). The blue curve reveals  $I_{DS}$  behavior when  $V_{GS}$  was applied; the red one shows  $I_{DS}$  obtained at  $V_{GS} = 0$  V, after the preapplied gate voltages were removed for 1 s. The arrows indicate the directions of the hysteresis loops. Energy-band diagrams for the FeFET device in the down-polarized state (d) and up-polarized state (e).

until  $-1.2$  kV/cm and saturates at  $-6.5$  kV/cm with backward sweeping. The coercive fields are about 2.75 and 2.4 kV/cm with forward sweeping and backward sweeping, respectively. The coercive field of PMN-PT is relatively low compared to other ferroelectric materials, for instance,  $\text{Pb}(\text{Zr}_{0.2}\text{Ti}_{0.8})\text{O}_3$ ,<sup>24</sup>  $\text{Hf}_{0.5}\text{Zr}_{0.5}\text{O}_2$ ,<sup>25</sup> and  $\text{P}(\text{VDF-TrFE})$ .<sup>30</sup> The coercive fields of  $\text{Pb}(\text{Zr}_{0.2}\text{Ti}_{0.8})\text{O}_3$ ,  $\text{Hf}_{0.5}\text{Zr}_{0.5}\text{O}_2$ , and  $\text{P}(\text{VDF-TrFE})$  are 50 kV/cm, 1.5 MV/cm, and 0.55 MV/cm, respectively. Note that the transport characteristics of MoS<sub>2</sub>-based FETs were carried out in vacuum ( $\sim 10^{-6}$  Torr). Figure 2c illustrates the output characteristic curves of MoS<sub>2</sub>/PMN-PT FeFETs. As the  $V_{DS}$  bias ranges from  $-1$  to  $+1$  V, the channel current  $I_{DS}$  shows a linear increase, suggesting a good ohmic contact between the MoS<sub>2</sub> channel and metal electrodes. The output characteristic curves of MoS<sub>2</sub> on the PMN-PT substrate are similar to those on the Si/SiO<sub>2</sub> substrate, as illustrated in the inset of Figure 2c. For the output curves, when a negative  $V_{GS}$  bias is applied, the MoS<sub>2</sub> channel is in a high resistance state. The inset of Figure 2d presents the transfer characteristic curves of MoS<sub>2</sub> on the Si/SiO<sub>2</sub> substrate. As the scanned gate voltage sweeps from  $V_{GS} = -60$  to  $+80$  V, the MoS<sub>2</sub> conduction channel clearly shows a switch from the Off state to On state, indicating electron doping (*n*-type) in as-grown MoS<sub>2</sub> materials. Moreover, the hysteresis between the forward and reverse transfer characteristic curves is almost negligible. The transfer characteristic curve of MoS<sub>2</sub>/PMN-PT FeFETs measured at the  $V_{DS}$  of 0.1 V is presented in Figure 2d. The transport behavior reveals a large hysteresis, owing to a significant difference between the forward and reverse curves. The On-Off ratio was observed to be  $\approx 10^6$  at  $V_{GS} = 0$  V, indicating the feasible application of MoS<sub>2</sub>/PMN-PT FeFETs for non-volatile memory.

It is worth noting that the gate dielectric layer has a significant impact on the charge concentration and con-

ductance of the MoS<sub>2</sub> channel. In other words, the doping concentration in the channel is in direct proportion to the dielectric constant of the gate insulator. Nevertheless, it is inversely corrected with the thickness of the dielectric layer under the same  $V_{GS}$ . At room temperature, the dielectric constant of PMN-PT has a value of  $\sim 5000$ , which is over 3 orders-of-magnitude more than the value of  $\sim 3$  for SiO<sub>2</sub>. However, compared to SiO<sub>2</sub> with a thickness of 300 nm, in this work, the PMN-PT substrate has a larger thickness of 0.5 mm. As a result, PMN-PT and SiO<sub>2</sub> have comparable doping effects on MoS<sub>2</sub> under the identical  $V_{GS}$ . Additionally, it is worth noting that PMN-PT also has a piezoelectric effect. Therefore, the electric field can provide polarization and in-plane strain simultaneously. The induced in-plane strain could be possibly transmitted to the above MoS<sub>2</sub> layer. Thus, in the case of employing PMN-PT as a gate insulator, there may be two possible coexisting tuning mechanisms, namely, the polarization effect and strain effect. To verify the possibility, the in-plane strain supplied by the PMN-PT was measured. As shown in Figure S1, the strain is much smaller, less than 0.1% for  $E_{GS}$  of 3 kV/cm. However, at least a 5% strain is required to induce the obvious change in band structure of MoS<sub>2</sub>.<sup>42</sup> Therefore, the strain effects on the FeFET are negligible and ruled out in this research.

To further research the modulation of transport properties for MoS<sub>2</sub> by PMN-PT, the transfer characteristic curves at different  $E_{GS}$  scales were measured (see Figure S2). For  $E_{GS\text{max}} = 1.4$  and 2 kV/cm, in which the spontaneous polarization of PMN-PT does not reverse, the ferroelectric  $P$  of PMN-PT shows a slight hysteresis loop.<sup>36</sup> The transport properties of MoS<sub>2</sub> have a similar shape with the ferroelectric hysteresis loop of PMN-PT. When  $E_{GS\text{max}}$  exceeds the  $E_C$ , the  $I_{DS}$ - $E_{GS}$  curve has a consistent hysteresis loop with the ferroelectric hysteresis loop as illustrated in Figure 2b. The clockwise direction of the

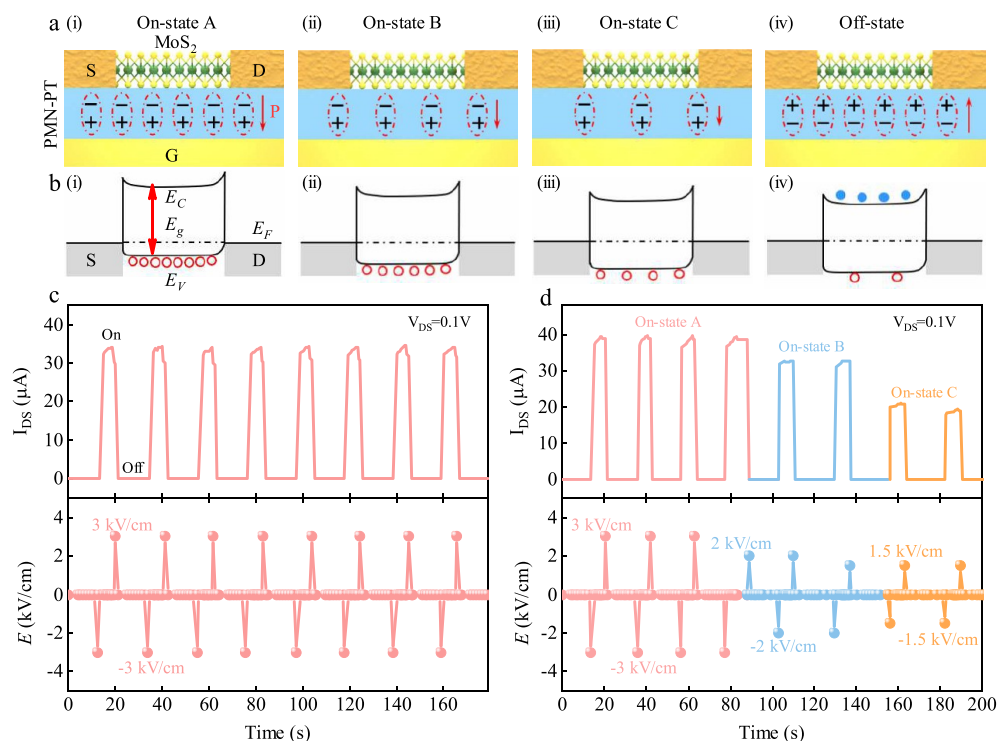


**Figure 4.** (a) Polarization bound charge distribution of FE gating operation in a FeFET device and (b) the corresponding energy band diagrams. Blue and red circles represent electrons and holes, respectively. (c) Switching operations of the FeFET device as a function of pulse electric fields ( $E = \pm 3$  kV/cm) imposed on the PMN–PT. (d) Multilevel nonvolatile switching of the FeFET device at room temperature between four states under electric field pulses.

observed hysteresis in the MoS<sub>2</sub>/PMN–PT FeFETs shown in Figure 2d is opposite to the counterclockwise direction of polarization hysteresis for PMN–PT. Two primary factors can affect the transport properties of MoS<sub>2</sub>. The first one is ferroelectric polarization, which tunes the transport properties of MoS<sub>2</sub> via the mutual effect between MoS<sub>2</sub> and the ferroelectric dielectric layer, and another factor is the existence of interface charge traps.<sup>36</sup> The interplay between interface charge traps and the ferroelectric polarization can be answerable for the clockwise hysteresis behaviors. As a typical oxide ferroelectric material, in the region near the interface between MoS<sub>2</sub> and PMN–PT, there are oxygen deficiencies. These defects could act as electron traps that can dynamically respond to the change of the ferroelectric polarization induced built-in field under different  $V_{GS}$  values. In addition, the oxygen/water molecules in the ambient absorbed on the surface of PMN–PT before MoS<sub>2</sub> transferred onto it also contribute to the defects in the interfacial layer. The water molecules located at MoS<sub>2</sub> and PMN–PT can screen the polarization.<sup>46</sup> Owing to charge injection and polarization screening, the transport properties of MoS<sub>2</sub>/PMN–PT FeFETs are elusive.

In order to split the intrinsic ferroelectric contributions from the external charge traps on MoS<sub>2</sub> conductivity, we used a time-dependent measurement.<sup>32,37</sup> The detailed process is summarized in Figure 3a. First, an electric field of  $E_{GS} = 3$  kV/cm was applied for 500 ms, leading to the upward polarization of PMN–PT, and the  $I_{DS}$  was measured at the same time. The resulting  $I_{DS}$  of 30  $\mu$ A is caused by a combination of polarization and interfacial charges. Then, the applied electric field to PMN–PT was removed, and the  $I_{DS}$  was measured after 1 s again without the gate voltage applied. The measured

$I_{DS}$  without  $E_{GS}$  was  $2.7 \times 10^{-4}$   $\mu$ A, decreasing by 5 orders of magnitude, compared with the value when  $E_{GS}$  was implemented. In this way, when  $E_{GS}$  swept from 3 to  $-3$  kV/cm and back, two  $I_{DS}$  values were obtained at each gate voltage. Therefore, two transfer characteristic curves were acquired, as presented in Figure 3c. The hysteresis loop obtained at  $\tau_{wait} = 0$  s represents the joint effect of the ferroelectric polarization and interface charge traps on the conductance of the MoS<sub>2</sub> channel. The hysteresis loop observed at  $\tau_{wait} = 1$  s after the interfacial charges dissipate shows that the conductivity of MoS<sub>2</sub> is mainly tuned via the ferroelectric polarization of PMN–PT. It is unclear to which extent the interfacial charges have dissipated in 1 s. Therefore, the same measurement procedure was used to study the transport behavior of the same MoS<sub>2</sub>/PMN–PT FeFET at  $\tau_{wait} = 5, 10,$  and  $20$  s. A series of polarization-controlled transport hysteresis loops measured at different  $\tau_{wait}$  values was illustrated in Figure S3. These data show that longer  $\tau_{wait}$  results in further evolution of the hysteresis shape. However, these changes are rather small between the transformations of the hysteresis at different  $\tau_{wait}$  values.

The hysteresis loops observed at  $\tau_{wait} = 0$  and  $1$  s are dramatically different as shown in Figure 3c. Once the impact of the charge traps is depleted, the conductivity of MoS<sub>2</sub>/PMN–PT FeFET changes from  $n$ -type to  $p$ -type. In previous reports,  $p$ -type MoS<sub>2</sub> can be observed through high work function contacts<sup>38,39</sup> and chemical doping.<sup>40</sup> In this work, the  $p$ -type MoS<sub>2</sub> may be caused by the dangling bond on the surface of PMN–PT, which gets filled via capturing electrons from the MoS<sub>2</sub> valence band, making the Fermi energy lie slightly below the valence band maximum.<sup>41</sup> After a negative  $E_{GS}$  pulse is applied, the measured  $I_{DS}$  has a dramatic increase

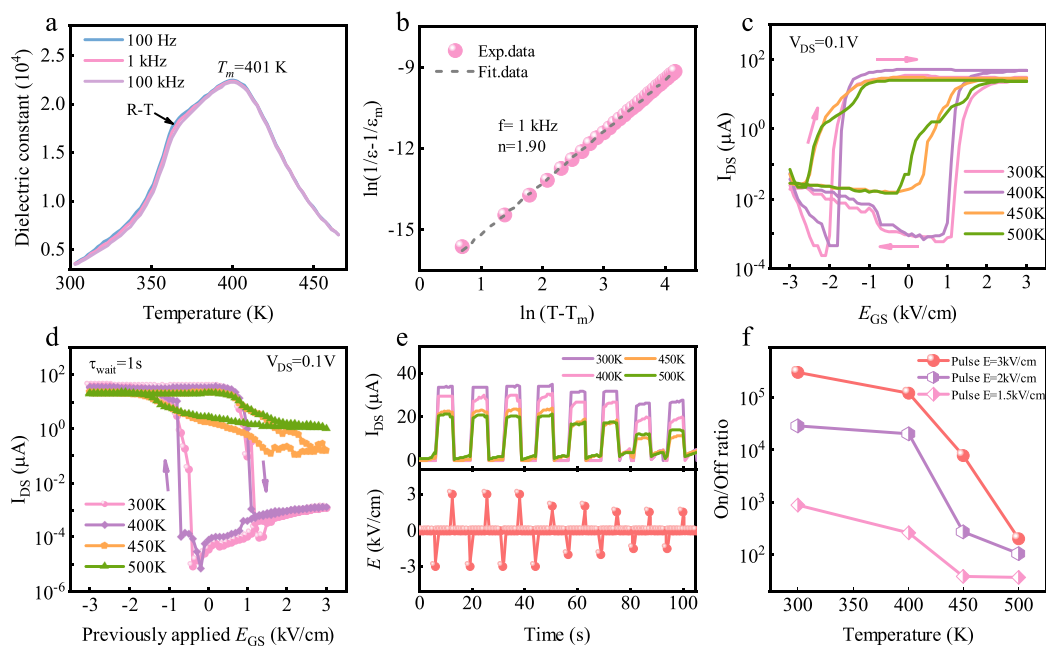


**Figure 5.** (a) Temperature-dependent dielectric permittivity of the PMN–PT single crystal. (b) The  $\ln(1/\epsilon - 1/\epsilon_m)$  curve as a function of  $\ln(T - T_m)$ . (c) Electrical transfer curves while  $V_{GS}$  was applied and (d)  $I_{DS}$  measured at grounded  $V_{GS} = 0$  V, after the preapplied gate voltages were removed for 1 s of the FeFET device under different temperatures ranging from 300 to 500 K. (e) Measurement-temperature-dependent multilevel nonvolatile switching of the FeFET device. (f) On–Off channel current ratio with different sets of pulse electric fields as a function of temperature.

as presented in Figure 3b. The value of  $I_{DS}$  increases with an increase in the applied electric field. On the contrary, when the PMN–PT is up-polarized toward to the channel layer, the conductance of the channel decreases, smaller than the original state. The nonvolatile On and Off states is of importance for memory applications of the MoS<sub>2</sub>/PMN–PT FeFETs. The simple model for FE gating operation in the FeFETs illustrated in Figure 3d,e is used to explain how the FE gating can tune the channel current. The *p*-type conductivity of MoS<sub>2</sub> indicates that holes are the majority carriers. Therefore, when the PMN–PT is down-polarized by a negative bias, the top surface of PMN–PT is negatively charged; accordingly, the MoS<sub>2</sub> flake is positively charged. Thus, the accumulation of holes can induce a *p*-type doping in the MoS<sub>2</sub> channel. In contrast, when a positive  $E_{GS}$  exceeding coercive field is implemented to the PMN–PT, the polarization direction of PMN–PT is up-polarized. Hence, the depletion of holes in the MoS<sub>2</sub> channel gives rise to the reduced conductivity of MoS<sub>2</sub>.

To shed light on the working principle of the FeFET and how the conductance of the channel can be tuned by the PMN–PT gating at different  $E_{GS}$  values, in Figure 4a,b, we raise device working schematics and band diagrams to interpret the effect of the ferroelectric polarization under different  $E_{GS}$  values. The remanent polarization  $2P_r$  of PMN–PT in this work is about  $36 \mu\text{C}/\text{cm}^2$ , and the corresponding surface charge density induced by the polarization switch can reach  $2.25 \times 10^{14}/\text{cm}^2$ . If these charges are not counteracted by interfacial states or traps, the value denotes the upper limit areal density of carriers accumulated or depleted in the 2D channel. In the device with back-gate configuration, where degenerately doped Si and 270 nm SiO<sub>2</sub> serve as the substrate and back-gate, respectively, the carrier concentration  $n_{2D}$  of single-layer MoS<sub>2</sub> is about  $3.6 \times 10^{12}/\text{cm}^2$  at a particular doping level.<sup>43</sup> This value is 2 orders of magnitude lower than that of the polarization charge. Thus, a remarkable modulation of carrier density would be observed when PMN–PT single

crystals are employed as the gate dielectric layer. Due to the significant difference in the conductivity of MoS<sub>2</sub> under two polarization states at  $E_{GS} = 0$  kV/cm, the channel conductivity can be tuned by applying  $E = \pm 3$  kV/cm pulse electric fields to the PMN–PT in an invertible, nonvolatile, and reproducible way. Figure 4c presents representative  $I_{DS}$ –time plots recorded from MoS<sub>2</sub>–PMN–PT FeFETs. When a negative pulsed field exceeding  $-2.4$  kV/cm is first applied to PMN–PT, a low resistance state (On state) can be accomplished after the negative pulsed field is removed. In this study,  $E_{GS} = -3$  kV/cm was selected. Conversely, a high resistance state (Off state) can be realized when  $E_{GS} = 3$  kV/cm was used. The On/Off ratio measured at  $E_{GS} = 0$  kV/cm is about  $10^6$ , which is at least 2 orders of magnitude higher compared to previous reports.<sup>24,32</sup> The On and Off currents remain unchanged in Figure 4c, indicating the stable memory operation. While the cycle endurance of MoS<sub>2</sub>/PMN–PT memory is depicted in Figure 4c, the actual On/Off ratio may vary as a function of the durations of  $E_{GS}$  and  $\tau_{\text{wait}}$ .<sup>24</sup> Moreover, by adjusting the amplitude of the electric fields (2 and 1.5 kV/cm), one can realize the other hysteresis loops of conductivity with the intermediate states B and C, which relate to the electric field. Therefore, the conductivity of the MoS<sub>2</sub> channel can be switched between these four nonvolatile states by applying appropriate electric field pulses, as illustrated in Figure 4d. When one controls the amplitude of the electric field pulses from 3 to 2 or 1.5 kV/cm, the On state is switched from A to B or C. From a practical perspective, the stability of the three On states is a crucial factor for a memory device to maintain functionality. Therefore, the retention property of the MoS<sub>2</sub>–PMN–PT FeFET has been characterized for the memory application. The retention characteristic of the four nonvolatile states is shown in Figure S4. There is no obvious decay of the four states for as long as 6000 s. The present results suggest a novel application in high-density, multifunction, and multilevel integrated memories.

As discussed above, the electrical properties of MoS<sub>2</sub>/PMN–PT FeFETs are modulated by the interface charge traps and ferroelectric polarization. In this study, time-dependent measurements were employed to distinguish the effect of ferroelectric polarization from the interface charge traps. The effect of charge traps still can not be ruled out completely, due to the fact that some residual charges remain at the MoS<sub>2</sub>/PMN–PT interface even after  $\tau_{\text{wait}} = 5$  min.<sup>32</sup> In order to investigate intuitively how ferroelectric polarization can affect the transport behaviors of MoS<sub>2</sub>, temperature-dependent transport and hysteresis behaviors of the MoS<sub>2</sub>/PMN–PT device have been investigated. As we know, for normal ferroelectric materials, at  $T = T_C$  (Curie temperature), the phase changes from a ferroelectric phase to paraelectric one. Ferroelectric polarization is no longer in existence in the paraelectric phase. To obtain the  $T_m$  (temperature corresponding to the maximum dielectric constant) of the PMN–PT single crystal, dielectric properties were measured at 100 Hz, 1 kHz, and 100 kHz in the temperature range of 300 to 470 K, as depicted in Figure 5a. The measured  $T_m$  of PMN–PT is around 401 K. From Figure 5a, we can see that  $\epsilon$  has a peak near  $T_m = 401$  K; at that temperature, the phase of PMN–PT transforms from the tetragonal phase (ferroelectric phase) to the cubic phase (paraelectric phase). The phase transition between the rhombohedral and tetragonal phase occurs at 366 K. For both transitions mentioned above, the frequency dispersion and diffusion phase transition are all weak, suggesting that the dielectric behavior looks like normal ferroelectrics. However, the frequency dispersion still exists ( $T > T_m$ ), which is different from normal ferroelectrics. To study the relaxor characteristic above  $T_m$ , the relationship between  $\epsilon$  and  $T$  should be written as

$$\left(\frac{1}{\epsilon} - \frac{1}{\epsilon_m}\right)^{1/n} = \frac{T - T_m}{C'} \quad (1)$$

where  $\epsilon_m$  is the value of the dielectric constant at  $T_m$  and  $n$  and  $C'$  are constants. The parameter  $n$  ( $1 \leq n \leq 2$ ) represents the diffuseness exponent and gauges the degree of dielectric relaxation of relaxor ferroelectrics. For  $n = 1$ , eq 1 corresponds to the Curie–Weiss law of normal ferroelectrics. In an extreme case, when  $n = 2$ , eq 1 is for relaxor ferroelectrics.<sup>44</sup> Figure 5b illustrates the relationship between  $\ln(1/\epsilon - 1/\epsilon_m)$  and  $\ln(T - T_m)$  of PMN–PT. In this work, the value of  $n$  is observed to be 1.9 for the PMN–PT, suggesting the relaxor feature of PMN–PT when  $T > T_m$ .

Figure 5c presents the  $I_{\text{DS}}-E_{\text{GS}}$  curves while  $E_{\text{GS}}$  was applied, with the temperature ranging from 300 to 500 K. Each cyclic electric field is repeated sweeping from  $-E_{\text{GSmax}}$  to  $E_{\text{GSmax}}$  to  $-E_{\text{GSmax}}$ . Under different temperatures, the resultant hysteresis loops reveal good reproducibility. As discussed above, the clockwise hysteresis behaviors, which are opposite to the counterclockwise hysteresis behaviors of ferroelectric polarization, can be ascribed to joint effects of interface charge traps and ferroelectric polarization. The possible factors affecting the temperature-dependent electrical performances of the MoS<sub>2</sub>/PMN–PT device may be the polarization of PMN–PT, the carrier transport characteristics in the MoS<sub>2</sub> channel, and interface charge traps in the interface between the MoS<sub>2</sub> flake and PMN–PT. In order to determine the crucial factor, the related temperature-dependent measurements have been discussed below.

The hysteresis loop in the PMN–PT single crystal between the polarization  $P$  and  $E$  in the temperature range of 300–450 K has been investigated.<sup>44</sup> It has been reported that with an increase in the temperature the remnant polarization ( $P_r$ ) slightly increases, until the critical temperature is reached. A sharp decrease of  $P_r$  is observed near  $T_m$ . However, when the temperature goes from 300 to 400 K, the maximum drain current ( $I_{\text{DS}}$ ) has a significant increase, which is opposite from the change of the polarization of PMN–PT with increasing temperature. Therefore, there are other temperature-dependent factors playing a major role. When one considers the effect of carrier transport characteristics in the MoS<sub>2</sub> channel, the scattering mechanism has been regarded as a critical factor. At temperatures below 100 K, the mobility of MoS<sub>2</sub> is restricted by the Coulomb scattering mechanism; nevertheless, at higher temperatures (above 100 K), the mobility restricted by phonon–electron scattering decreases with an increase in the temperature.<sup>45</sup> Thus, the current of MoS<sub>2</sub> should be reduced with the enhancement of phonon scattering with an increase in the temperature. However, the current of MoS<sub>2</sub> increases as temperature goes up from 150 to 400 K, as shown in Figure 5Sb. Although the current of MoS<sub>2</sub> shows a declining trend as the temperature rises further above 400 K, the value of the maximum current at 500 K is compared to that of room temperature. Therefore, it is the interfacial charge traps that contribute to the enlargement of transport and hysteresis behaviors of MoS<sub>2</sub>/PMN–PT FeFETs. The charge trapping process has strong temperature dependence, and it is suppressed at low temperature, which is related to the thermal activation.<sup>21,46</sup> The dynamic process of charge trapping/detrapping will become more drastic at a faster speed with an increase in the temperature. Under the polarization, the current hysteresis loop induced by interfacial charge trapping/detrapping will be increased with the increase of temperature.

To deeply investigate the influence of ferroelectric polarization on the electrical properties for MoS<sub>2</sub>/PMN–PT FeFETs, the time-dependent measurements were employed in the temperature range of 300 to 500 K. In Figure 5d, where the effect of charge traps is minimized, the trend of the current is consistent with that of ferroelectric polarization of PMN–PT with an increase in the temperature. Moreover, to understand deeply the dependence of the switching operation on ferroelectric polarization, three representative  $I_{\text{DS}}$  curves of On and Off states versus time were observed in the temperature range from 300 to 500 K, as illustrated in Figure 5e. Along with an increase in the temperature, the On and Off currents have the quasi-static trend for FeFET operation, as shown in Figure 5d. The effect of ferroelectric polarization is further confirmed by the temperature-dependent electrical performances of MoS<sub>2</sub>/PMN–PT FeFETs. As displayed in Figure 5f, the On–Off ratios of three pulse electric fields applied to PMN–PT are observed to decrease dramatically when the temperature goes up above the Curie value. For electric field pulses whose amplitudes are 3 and 2 kV/cm with an increase in the temperature, the On–Off ratios reduce by 3 orders of magnitude. What is noteworthy is that, at temperatures above the Curie temperature, the hysteresis loops of transfer curves and On–Off ratios still exist. For relaxor ferroelectrics, the randomly oriented polar microregions are formed in paraelectric crystals. The polar microregions may remain even at hundreds of degrees above the Curie temperature. The polar microregions are in

dynamical disorder above the Curie temperature, resulting in a weak remnant polarization.

#### 4. CONCLUSIONS

In summary, FeFET devices comprising 2D MoS<sub>2</sub> channels with monocrystal PMN–PT substrate have been demonstrated. The MoS<sub>2</sub>–PMN–PT FeFET devices have a large electronic hysteresis and promising nonvolatile memory properties. The clockwise hysteresis behaviors of FeFETs have been demonstrated to be induced by the combined effects between interface charge traps and ferroelectric polarization. A reversed polarization dependence of the hysteresis electronic transport can be observed, when the influence of the interface charge traps is dissipated. Our prototype FeFETs exhibit multiple conductance states with high On–Off ratios ( $\sim 10^6$ ) by modulating the polarized states of the PMN–PT gate insulator. The retention characteristic of the four nonvolatile states indicates that no obvious decay of the four states is observed for as long as 6000 s. Furthermore, temperature-dependent electrical performances have been investigated, analyzing the specific effects of interface charge traps and ferroelectric polarization. These results suggest that hybrid 2D semiconductor–ferroelectric structures may open up opportunities for developing high-density and nonvolatile multilevel memories.

#### ■ ASSOCIATED CONTENT

##### Supporting Information

The Supporting Information is available free of charge at <https://pubs.acs.org/doi/10.1021/acsami.0c09951>.

In-plane strain curve for the (001)-oriented PMN–PT crystal (Figure S1); the transfer characteristic curves of MoS<sub>2</sub>–PMN–PT FeFETs (Figures S2 and S3); data retention characteristics of MoS<sub>2</sub>–PMN–PT FeFETs (Figure S4); measurement-temperature-dependent transport properties of MoS<sub>2</sub>–PMN–PT FeFETs in the range from 150 to 300 K (Figure S5) (PDF)

#### ■ AUTHOR INFORMATION

##### Corresponding Authors

**Jinzhong Zhang** – Technical Center for Multifunctional Magneto-Optical Spectroscopy (Shanghai), Engineering Research Center of Nanophotonics & Advanced Instrument (Ministry of Education), Department of Materials, School of Physics and Electronic Science, East China Normal University, Shanghai 200241, China; Phone: +86-21-54345150; Email: [jzzhang@ee.ecnu.edu.cn](mailto:jzzhang@ee.ecnu.edu.cn); Fax: +86-21-54342933

**Zhigao Hu** – Technical Center for Multifunctional Magneto-Optical Spectroscopy (Shanghai), Engineering Research Center of Nanophotonics & Advanced Instrument (Ministry of Education), Department of Materials, School of Physics and Electronic Science, East China Normal University, Shanghai 200241, China; Collaborative Innovation Center of Extreme Optics, Shanxi University, Taiyuan, Shanxi 030006, China; Shanghai Institute of Intelligent Electronics & Systems, Fudan University, Shanghai 200433, China; [orcid.org/0000-0003-0575-2191](https://orcid.org/0000-0003-0575-2191); Phone: +86-21-54345150; Email: [zg hu@ee.ecnu.edu.cn](mailto:zg hu@ee.ecnu.edu.cn); Fax: +86-21-54342933

##### Authors

**Liping Xu** – Technical Center for Multifunctional Magneto-Optical Spectroscopy (Shanghai), Engineering Research Center

of Nanophotonics & Advanced Instrument (Ministry of Education), Department of Materials, School of Physics and Electronic Science, East China Normal University, Shanghai 200241, China

**Zhihua Duan** – Key Laboratory of Optoelectronic Material and Device, Department of Physics, Shanghai Normal University, Shanghai 200234, China

**Peng Zhang** – School of Materials Science & Engineering, Beihang University, Beijing 100191, China

**Xiang Wang** – Technical Center for Multifunctional Magneto-Optical Spectroscopy (Shanghai), Engineering Research Center of Nanophotonics & Advanced Instrument (Ministry of Education), Department of Materials, School of Physics and Electronic Science, East China Normal University, Shanghai 200241, China

**Liyan Shang** – Technical Center for Multifunctional Magneto-Optical Spectroscopy (Shanghai), Engineering Research Center of Nanophotonics & Advanced Instrument (Ministry of Education), Department of Materials, School of Physics and Electronic Science, East China Normal University, Shanghai 200241, China

**Kai Jiang** – Technical Center for Multifunctional Magneto-Optical Spectroscopy (Shanghai), Engineering Research Center of Nanophotonics & Advanced Instrument (Ministry of Education), Department of Materials, School of Physics and Electronic Science, East China Normal University, Shanghai 200241, China

**Yawei Li** – Technical Center for Multifunctional Magneto-Optical Spectroscopy (Shanghai), Engineering Research Center of Nanophotonics & Advanced Instrument (Ministry of Education), Department of Materials, School of Physics and Electronic Science, East China Normal University, Shanghai 200241, China; [orcid.org/0000-0001-8776-5687](https://orcid.org/0000-0001-8776-5687)

**Liangqing Zhu** – Technical Center for Multifunctional Magneto-Optical Spectroscopy (Shanghai), Engineering Research Center of Nanophotonics & Advanced Instrument (Ministry of Education), Department of Materials, School of Physics and Electronic Science, East China Normal University, Shanghai 200241, China

**Yongji Gong** – School of Materials Science & Engineering, Beihang University, Beijing 100191, China; [orcid.org/0000-0003-1432-6813](https://orcid.org/0000-0003-1432-6813)

**Junhao Chu** – Technical Center for Multifunctional Magneto-Optical Spectroscopy (Shanghai), Engineering Research Center of Nanophotonics & Advanced Instrument (Ministry of Education), Department of Materials, School of Physics and Electronic Science, East China Normal University, Shanghai 200241, China; Collaborative Innovation Center of Extreme Optics, Shanxi University, Taiyuan, Shanxi 030006, China; Shanghai Institute of Intelligent Electronics & Systems, Fudan University, Shanghai 200433, China

Complete contact information is available at: <https://pubs.acs.org/doi/10.1021/acsami.0c09951>

##### Author Contributions

<sup>†</sup>L.X. and Z.D. contributed equally. The experiments were conceived and managed by Z.H. The fabrication of the devices and the corresponding electrical measurements were performed by L.X. The temperature-dependent dielectric constant and the P–E measurements of the monocrystal PMN–PT were performed by Z.D. The MoS<sub>2</sub> samples were synthesized by P.Z. The AFM measurements were performed by X.W. L.X.,

Z.D., J.Z., and L.S. performed the data analysis. K.J., Y.L., L.Z., Y.G., and J.C. assisted with data analysis and the explanation. The manuscript was written and completed by all authors.

## Notes

The authors declare no competing financial interest.

## ACKNOWLEDGMENTS

This work was financially supported by the National Natural Science Foundation of China (Grants Nos. 91833303, 61974043, and 61674057), the National Key Research and Development Program of China (Grants Nos. 2018YFB0406500, 2017YFA0303403, and 2019YFB2203400), Projects of Science and Technology Commission of Shanghai Municipality (Grant Nos. 18JC1412400, 18YF1407000, 18YF1407200, and 19511120100), and the Program for Professor of Special Appointment (Eastern Scholar) at Shanghai Institutions of Higher Learning.

## REFERENCES

- (1) Okada, M.; Sawazaki, T.; Watanabe, K.; Taniguchi, T.; Hibino, H.; Shinohara, H.; Kitaura, R. Direct Chemical Vapor Deposition Growth of WS<sub>2</sub> Atomic Layers on Hexagonal Boron Nitride. *ACS Nano* **2014**, *8*, 8273–8277.
- (2) Feng, Q.; Zhu, Y.; Hong, J.; Zhang, M.; Duan, W.; Mao, N.; Wu, J.; Xu, H.; Dong, F.; Lin, F.; Jin, C.; Wang, C.; Zhang, J.; Xie, L. Growth of Large-Area 2D MoS<sub>2</sub>(1-x)Se<sub>2x</sub> Semiconductor Alloys. *Adv. Mater.* **2014**, *26*, 2648–2653.
- (3) Ma, R.; Zhang, H.; Yoo, Y.; Degregorio, Z. P.; Jin, L.; Golani, P.; Ghasemi Azadani, J.; Low, T.; Johns, J. E.; Bendersky, L. A.; Davydov, A. V.; Koester, S. J. MoTe<sub>2</sub> Lateral Homojunction Field-Effect Transistors Fabricated Using Flux-Controlled Phase Engineering. *ACS Nano* **2019**, *13*, 8035–8046.
- (4) Hoffman, A. N.; Stanford, M. G.; Zhang, C.; Ivanov, I. N.; Oyedele, A. D.; Sales, M. G.; McDonnell, S. J.; Koehler, M. R.; Mandrus, D. G.; Liang, L.; Sumpter, B. G.; Xiao, K.; Rack, P. D. Atmospheric and Long-Term Aging Effects on the Electrical Properties of Variable Thickness WSe<sub>2</sub> Transistors. *ACS Appl. Mater. Interfaces* **2018**, *10*, 36540–36548.
- (5) Wang, F.; Gao, T.; Zhang, Q.; Hu, Z. Y.; Jin, B.; Li, L.; Zhou, X.; Li, H.; Van Tendeloo, G.; Zhai, T. Liquid-Alloy-Assisted Growth of 2D Ternary Ga<sub>2</sub>In<sub>3</sub>S<sub>9</sub> toward High-Performance Uv Photodetection. *Adv. Mater.* **2019**, *31*, 1806306.
- (6) Chang, Y. H.; Zhang, W. J.; Zhu, Y. H.; Han, Y.; Pu, J.; Chang, J.-K.; Hsu, W.-T.; Huang, J.-K.; Hsu, C.-L.; Chiu, M.-H.; Takenobu, T.; Li, H. N.; Wu, C.; Chang, W. H.; Wee, A. T. S.; Li, L. J. Monolayer MoSe<sub>2</sub> Grown by Chemical Vapor Deposition for Fast Photodetection. *ACS Nano* **2014**, *8*, 8582–8590.
- (7) Tan, C.; Zhang, H. Two-Dimensional Transition Metal Dichalcogenide Nanosheet-Based Composites. *Chem. Soc. Rev.* **2015**, *44*, 2713–2731.
- (8) Zhang, H. Ultrathin Two-Dimensional Nanomaterials. *ACS Nano* **2015**, *9*, 9451–9469.
- (9) Chen, X.; Lu, X.; Deng, B.; Sinai, O.; Shao, Y.; Li, C.; Yuan, S.; Tran, V.; Watanabe, K.; Taniguchi, T.; Naveh, D.; Yang, L.; Xia, F. Widely Tunable Black Phosphorus Mid-Infrared Photodetector. *Nat. Commun.* **2017**, *8*, 1672.
- (10) Li, A.; Chen, Q.; Wang, P.; Gan, Y.; Qi, T.; Wang, P.; Tang, F.; Wu, J. Z.; Chen, R.; Zhang, L.; Gong, Y. Ultrahigh-Sensitive Broadband Photodetectors Based on Dielectric Shielded MoTe<sub>2</sub>/Graphene/SnS<sub>2</sub> P-G-N Junctions. *Adv. Mater.* **2019**, *31*, 1805656.
- (11) Lu, Q.; Yu, Y.; Ma, Q.; Chen, B.; Zhang, H. 2d Transition-Metal-Dichalcogenide-Nanosheet-Based Composites for Photocatalytic and Electrocatalytic Hydrogen Evolution Reactions. *Adv. Mater.* **2016**, *28*, 1917–1933.
- (12) Huang, X.; Zeng, Z.; Bao, S.; Wang, M.; Qi, X.; Fan, Z.; Zhang, H. Solution-Phase Epitaxial Growth of Noble Metal Nanostructures on Dispersible Single-Layer Molybdenum Disulfide Nanosheets. *Nat. Commun.* **2013**, *4*, 1444.
- (13) Shi, J.; Wang, X.; Zhang, S.; Xiao, L.; Huan, Y.; Gong, Y.; Zhang, Z.; Li, Y.; Zhou, X.; Hong, M.; Fang, Q.; Zhang, Q.; Liu, X.; Gu, L.; Liu, Z.; Zhang, Y. Two-Dimensional Metallic Tantalum Disulfide as a Hydrogen Evolution Catalyst. *Nat. Commun.* **2017**, *8*, 958.
- (14) Cui, X.; Kong, Z.; Gao, E.; Huang, D.; Hao, Y.; Shen, H.; Di, C. A.; Xu, Z.; Zheng, J.; Zhu, D. Rolling up Transition Metal Dichalcogenide Nanoscrolls Via One Drop of Ethanol. *Nat. Commun.* **2018**, *9*, 1301.
- (15) Guo, S.; Yang, D.; Zhang, S.; Dong, Q.; Li, B.; Tran, N.; Li, Z.; Xiong, Y.; Zaghoul, M. E. Development of a Cloud-Based Epidermal MoSe<sub>2</sub> Device for Hazardous Gas Sensing. *Adv. Funct. Mater.* **2019**, *29*, 1900138.
- (16) Xu, L.; Zhang, P.; Jiang, H.; Wang, X.; Chen, F.; Hu, Z.; Gong, Y.; Shang, L.; Zhang, J.; Jiang, K.; Chu, J. Large-Scale Growth and Field-Effect Transistors Electrical Engineering of Atomic-Layer SnS<sub>2</sub>. *Small* **2019**, *15*, 1904116.
- (17) Zhou, J.; Lin, J.; Huang, X.; Zhou, Y.; Chen, Y.; Xia, J.; Wang, H.; Xie, Y.; Yu, H.; Lei, J.; Wu, D.; Liu, F.; Fu, Q.; Zeng, Q.; Hsu, C. H.; Yang, C.; Lu, L.; Yu, T.; Shen, Z.; Lin, H.; Yakobson, B. I.; Liu, Q.; Suenaga, K.; Liu, G.; Liu, Z. A Library of Atomically Thin Metal Chalcogenides. *Nature* **2018**, *556*, 355–361.
- (18) Park, H.; Shin, G. H.; Lee, K. J.; Choi, S.-Y. Probing Temperature-Dependent Interlayer Coupling in a MoS<sub>2</sub>/h-BN Heterostructure. *Nano Res.* **2020**, *13*, 576–582.
- (19) Mak, K. F.; Lee, C.; Hone, J.; Shan, J.; Heinz, T. F. Atomically Thin MoS<sub>2</sub>: A New Direct-Gap Semiconductor. *Phys. Rev. Lett.* **2010**, *105*, 136805.
- (20) Noh, T.; Shin, H. S.; Seo, C.; Kim, J. Y.; Youn, J.; Kim, J.; Lee, K.-S.; Joo, J. Significant Enhancement of Photoresponsive Characteristics and Mobility of MoS<sub>2</sub>-Based Transistors through Hybridization with Perovskite CsPbBr<sub>3</sub> Quantum Dots. *Nano Res.* **2019**, *12*, 405–412.
- (21) Si, M.; Saha, A. K.; Gao, S.; Qiu, G.; Qin, J.; Duan, Y.; Jian, J.; Niu, C.; Wang, H.; Wu, W.; Gupta, S. K.; Ye, P. D. A Ferroelectric Semiconductor Field-Effect Transistor. *Nat. Electron.* **2019**, *2*, 580–586.
- (22) Huang, W.; Wang, F.; Yin, L.; Cheng, R.; Wang, Z.; Sendeku, M. G.; Wang, J.; Li, N.; Yao, Y.; He, J. Gate-Coupling-Enabled Robust Hysteresis for Nonvolatile Memory and Programmable Rectifier in Van Der Waals Ferroelectric Heterojunctions. *Adv. Mater.* **2020**, *32*, 1908040.
- (23) Mathews, S.; Ramesh, R.; Venkatesan, T.; Benedetto, J. Ferroelectric Field Effect Transistor Based on Epitaxial Perovskite Heterostructures. *Science* **1997**, *276*, 238–240.
- (24) Ko, C.; Lee, Y.; Chen, Y.; Suh, J.; Fu, D.; Suslu, A.; Lee, S.; Clarkson, J. D.; Choe, H. S.; Tongay, S.; Ramesh, R.; Wu, J. Ferroelectrically Gated Atomically Thin Transition-Metal Dichalcogenides as Nonvolatile Memory. *Adv. Mater.* **2016**, *28*, 2923.
- (25) Si, M.; Jiang, C.; Chung, W.; Du, Y.; Alam, M. A.; Ye, P. D. Steep-Slope WSe<sub>2</sub> Negative Capacitance Field-Effect Transistor. *Nano Lett.* **2018**, *18*, 3682–3687.
- (26) Si, M.; Liao, P. Y.; Qiu, G.; Duan, Y.; Ye, P. D. Ferroelectric Field-Effect Transistors Based on MoS<sub>2</sub> and CuInP<sub>2</sub>S<sub>6</sub> Two-Dimensional Van Der Waals Heterostructure. *ACS Nano* **2018**, *12*, 6700–6705.
- (27) Li, J.; Nagaraj, B.; Liang, H.; Cao, W.; Lee, C. H.; Ramesh, R. Ultrafast Polarization Switching in Thin-Film Ferroelectrics. *Appl. Phys. Lett.* **2004**, *84*, 1174.
- (28) Datta, R. S.; Syed, N.; Zavabeti, A.; Jannat, A.; Mohiuddin, M.; Rokunuzzaman, M.; Zhang, B. Y.; Aatur Rhman, M.; Atkin, P.; Messalea, K. A.; Ghasemian, M. B.; Gaspera, E. D.; Bhattacharyya, S.; Fuhrer, M. S.; Russo, S. P.; McConville, C. F.; Esrafizadeh, D.; Kalantar-Zadeh, K.; Daeneke, T. Flexible two-dimensional indium tin oxide fabricated using a liquid metal printing technique. *Nat. Electron.* **2020**, *3*, 51–58.

(29) Mayyas, M.; Li, H.; Kumar, P.; Ghasemian, M. B.; Yang, J.; Wang, Y.; Lawes, D. J.; Han, J.; Saborio, M. G.; Tang, J.; Jalili, R.; Lee, S. H.; Seong, W. K.; Russo, S. P.; Esrafilzadeh, D.; Daeneke, T.; Kaner, R. B.; Ruoff, R. S.; Kalantar-Zadeh, K. Liquid-Metal-Templated Synthesis of 2D Graphitic Materials at Room Temperature. *Adv. Mater.* **2020**, *32*, 2001997.

(30) Lee, H. S.; Min, S. W.; Park, M. K.; Lee, Y. T.; Jeon, P. J.; Kim, J. H.; Ryu, S.; Im, S. MoS<sub>2</sub> Nanosheets for Top-Gate Nonvolatile Memory Transistor Channel. *Small* **2012**, *8*, 3111–3115.

(31) Wang, X.; Wang, P.; Wang, J.; Hu, W.; Zhou, X.; Guo, N.; Huang, H.; Sun, S.; Shen, H.; Lin, T.; Tang, M.; Liao, L.; Jiang, A.; Sun, J.; Meng, X.; Chen, X.; Lu, W.; Chu, J. Ultrasensitive and Broadband MoS<sub>2</sub> Photodetector Driven by Ferroelectrics. *Adv. Mater.* **2015**, *27*, 6575–6581.

(32) Lipatov, A.; Sharma, P.; Gruverman, A.; Sinitskii, A. Optoelectrical Molybdenum Disulfide (MoS<sub>2</sub>)-Ferroelectric Memories. *ACS Nano* **2015**, *9*, 8089–8098.

(33) Sun, Y.; Xie, D.; Zhang, X.; Xu, J.; Li, X.; Li, X.; Dai, R.; Li, X.; Li, P.; Gao, X.; Zhu, H. Temperature-Dependent Transport and Hysteretic Behaviors Induced by Interfacial States in MoS<sub>2</sub> Field-Effect Transistors with Lead-Zirconate-Titanate Ferroelectric Gating. *Nanotechnology* **2017**, *28*, 045204.

(34) Li, H.; Zhang, Q.; Yap, C. C. R.; Tay, B. K.; Edwin, T. H. T.; Olivier, A.; Baillargeat, D. From Bulk to Monolayer MoS<sub>2</sub>: Evolution of Raman Scattering. *Adv. Funct. Mater.* **2012**, *22*, 1385–1390.

(35) Buscema, M.; Steele, G. M.; Van der Zant, H. S. J.; Castellanos-Gomez, A. The effect of the substrate on Raman and Photoluminescence emission of single-layer MoS<sub>2</sub>. *Nano Res.* **2014**, *7*, 561–571.

(36) Jie, W.; Hao, J. Time-Dependent Transport Characteristics of Graphene Tuned by Ferroelectric Polarization and Interface Charge Trapping. *Nanoscale* **2018**, *10*, 328–335.

(37) Baeumer, C.; Rogers, S. P.; Xu, R.; Martin, L. W.; Shim, M. Tunable Carrier Type and Density in Graphene/PbZr<sub>0.2</sub>Ti<sub>0.8</sub>O<sub>3</sub> Hybrid Structures through Ferroelectric Switching. *Nano Lett.* **2013**, *13*, 1693–1698.

(38) Chuang, S.; Battaglia, C.; Azcatl, A.; McDonnell, S.; Kang, J. S.; Yin, X.; Tosun, M.; Kapadia, R.; Fang, H.; Wallace, R. M.; Javey, A. MoS<sub>2</sub> p-Type Transistors and Diodes Enabled by High Work Function MoO<sub>x</sub> Contacts. *Nano Lett.* **2014**, *14*, 1337–1342.

(39) Min, S. W.; Yoon, M.; Yang, S. J.; Ko, K. R.; Im, S. Charge-Transfer-Induced p-Type Channel in MoS<sub>2</sub> Flake Field Effect Transistors. *ACS Appl. Mater. Interfaces* **2018**, *10*, 4206–4212.

(40) Nipane, A.; Karmakar, D.; Kaushik, N.; Karande, S.; Lodha, S. Few-Layer MoS<sub>2</sub> p-Type Devices Enabled by Selective Doping Using Low Energy Phosphorus Implantation. *ACS Nano* **2016**, *10*, 2128–2137.

(41) Dolui, K.; Rungger, I.; Sanvito, S. Origin of the n-type and p-type conductivity of MoS<sub>2</sub> monolayers on a SiO<sub>2</sub> substrate. *Phys. Rev. B: Condens. Matter Mater. Phys.* **2013**, *87*, 165402.

(42) Scalise, E.; Houssa, M.; Pourtois, G.; Afanasev, V.; Stesmans, A. Strain-Induced Semiconductor to Metal Transition in the Two-Dimensional Honeycomb Structure of MoS<sub>2</sub>. *Nano Res.* **2012**, *5*, 43–48.

(43) Radisavljevic, B.; Kis, A. Mobility Engineering and a Metal-Insulator Transition in Monolayer MoS<sub>2</sub>. *Nat. Mater.* **2013**, *12*, 815–820.

(44) Li, Z.; Xi, Z.; Xu, Z.; Yao, X. Dielectric/ferroelectric response and phase transition of PMN0.32PT single crystal. *J. Mater. Sci. Lett.* **2002**, *21*, 1325–1327.

(45) Jariwala, D.; Sangwan, V. K.; Late, D. J.; Johns, J. E.; David, V. P.; Marks, T. J.; Lauhon, L. J.; Hersam, M. C. Band-Like Transport in High Mobility Unencapsulated Single-Layer MoS<sub>2</sub> Transistors. *Appl. Phys. Lett.* **2013**, *102*, 173107.

(46) Wang, H.; Wu, Y.; Cong, C.; Shang, J.; Yu, T. Hysteresis of Electronic Transport in Graphene Transistors. *ACS Nano* **2010**, *4*, 7221–7228.